Neutron diffraction study on magnetic structures in a $La_{1.37}Sr_{1.63}Mn_2O_7$ single crystal under hydrostatic pressures of up to 0.8 GPa

Hirosuke Sonomura,[1,*] Tomoyuki Terai,[1,†] Tomoyuki Kakeshita,[1,‡] Toyotaka Osakabe,[2,§] and Kazuhisa Kakurai[2,‖]

[1]*Department of Materials Science and Engineering, Graduate School of Engineering, Osaka University, 2-1 Yamada-oka, Suita, Osaka 565-0871, Japan*

[2]*Quantum Beam Science Directorate, Japan Atomic Energy Agency 2-4 Shirakata-shirane, Tokai, Ibaraki 319-1195, Japan*

(Received 23 October 2012; revised manuscript received 19 February 2013; published 20 May 2013)

Magnetic structures in $La_{1.37}Sr_{1.63}Mn_2O_7$ single crystal under hydrostatic pressures of up to 0.8 GPa are investigated by neutron diffraction measurements to determine the magnetic phase diagram under hydrostatic pressure. The ground state is found to be a ferromagnetic ($FM_{uniaxial}$) structure under hydrostatic pressures of up to 0.8 GPa, in which the magnetic moments of Mn ions are parallel to the c axis. Under hydrostatic pressures of $P < 0.75$ GPa, the $FM_{uniaxial}$ structure changes to a canted antiferromagnetic (CAFM) structure at approximately 70 K and the CAFM structure directly changes to a paramagnetic (PM) structure at approximately 120 K. Under hydrostatic pressures of 0.75 GPa $\leqslant P \leqslant$ 0.8 GPa, the $FM_{uniaxial}$ structure changes to a CAFM structure at approximately 70 K, and the CAFM structure changes to a PM structure at approximately 120 K via an antiferromagnetic (AFM_{planar}) structure at approximately 95 K in which the magnetic moment lies in the ab plane. The relationship between the magnetic structure and the distortion of the MnO_6 octahedra is also discussed.

DOI: 10.1103/PhysRevB.87.184419 PACS number(s): 62.50.−p, 75.25.Dk, 75.30.Gw, 71.70.Ch

I. INTRODUCTION

The layered perovskite manganites $La_{2-2x}Sr_{1+2x}Mn_2O_7$ consist of a stacking of magnetic MnO_6 octahedra double layers and nonmagnetic (La, Sr) O monolayers having a rock-salt structure along the c axis.[1] These materials have attracted much interest because they exhibit fascinating phenomena such as a metal-insulator transition and colossal magnetoresistance which are closely related to their magnetic structure. The magnetic structure is induced by an anisotropic crystal structure and strong interplay between the charge, spin, and orbital degree of freedom of the Mn 3d electrons.[2–17] Such correlation between the orbital degree of freedom and the magnetic structure is also of interest from the perspective of orbitronics. In a previous study, Kubota *et al*. investigated the relationship between the magnetic structure and the distortion of MnO_6 octahedra in $La_{2-2x}Sr_{1+2x}Mn_2O_7$ ($0.3 \leqslant x \leqslant 0.5$) at 10 K by powder neutron diffraction measurement. They found that, as the concentration x increases, the magnetic structure changes from a ferromagnetic structure to an antiferromagnetic structure and the MnO_6 octahedra shrinks relatively along the c axis. From these results, they speculated that the change in the magnetic structure as the concentration x changes is due to shrinkage of the MnO_6 octahedra along the c axis caused by an increase in the occupancy of the x^2-y^2 orbital relative to the $3z^2$-r^2 orbital.

To confirm the relationship between the magnetic structure and the distortion of the MnO_6 octahedra, it is desirable to conduct experiments where the concentration x does not change. Application of hydrostatic pressure is one such method in which the hydrostatic pressure changes the distortion of the MnO_6 octahedra without changing the concentration x.[18] However, there have been few studies on the magnetic structure in $La_{2-2x}Sr_{1+2x}Mn_2O_7$ under hydrostatic pressure.

In this study, we therefore investigate the magnetic structures in a single-crystalline $La_{1.37}Sr_{1.63}Mn_2O_7$ ($x = 0.315$) under hydrostatic pressures up to 0.8 GPa by neutron diffraction measurement and discuss the relationship between magnetic structure and distortion of the MnO_6 octahedra.

II. EXPERIMENTAL METHODS

Single-crystalline $La_{2-2x}Sr_{1+2x}Mn_2O_7$ was grown using the floating-zone method. Details of the growth conditions are given elsewhere.[19] The composition of the single crystal was determined to be $x = 0.315$ by using an inductively coupled plasma-atomic emission spectrometer. Part of the single crystal was crushed into powder for x-ray measurement at room temperature, confirming that the grown single crystal consisted of a single phase (space group $I4/mmm$). The magnetic ordering temperature was found by susceptibility measurements to be 112 K, which is almost identical to the value reported previously.[16,17]

Neutron diffraction measurements to determine the magnetic structure were performed under ambient pressure and hydrostatic pressures of $P = 0.4, 0.6, 0.7, 0.75$, and 0.8 GPa. Neutron diffraction measurements of the single-crystalline specimen were performed using a triple-axis spectrometer at JRR-3M in JAEA. A nonpolarized beam with collimation series of 80′-80′-80′-80′ was used. The single-crystalline specimen was put in a 4K-GM refrigerator for the measurements under ambient pressure. For the measurements under hydrostatic pressure, the single-crystalline specimen and a single-crystalline NaCl reference specimen were encapsulated in a Cu-Be hydrostatic pressure cell and this cell was placed in a cryostat. The pressure-transmitting medium was a mixture of fluorinates (FC70:FC77 = 1:1) and the value of the pressure was estimated from the lattice parameter of the NaCl single crystal. The elastic scattering from ($h0l$) reflections was measured by ω-2θ scan in the temperature range of 4 K $\leqslant T \leqslant$ 160 K. Since the Bravais lattice is body-centered-tetragonal in the present system, reflections at $h + k + l = 2n$ (for integer n) arise from both nuclear and magnetic reflections from ferromagnetic structures. Consequently, the integrated intensity of magnetic

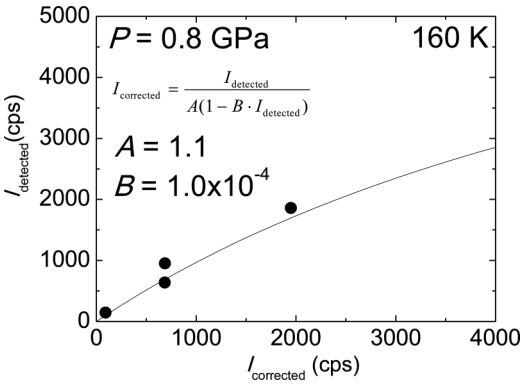

FIG. 1. Typical fitting result at 0.8 GPa for determining parameters A and B. The detected nuclear intensity at paramagnetic temperature (160 K) is fitted to the calculated nuclear intensity. In the figure, the dots and solid line represent the detected nuclear intensities and the calculated nuclear intensity, respectively.

reflections at $h + k + l = 2n$ is obtained by subtracting the integrated intensity of the paramagnetic phase at 160 K, at which point the integrated intensity arises from only the nuclear reflections. Reflections at $h + k + l = 2n + 1$ arise from only magnetic reflections from antiferromagnetic structures.

The single-crystalline specimen used in the present study did not have a measured mosaic structure. Consequently, we had to correct the detected intensity I_{detected} to account for the extinction effect. The relation between the corrected intensity $I_{\text{corrected}}$ and the detected intensity I_{detected} is given by[20]

$$I_{\text{corrected}} = \frac{I_{\text{detected}}}{A(1 - B \cdot I_{\text{detected}})}, \tag{1}$$

where A and B are parameters. These parameters were determined by fitting the detected nuclear intensity at paramagnetic temperature (160 K) to the calculated nuclear intensity. A typical fitting result for 0.8 GPa is shown in Fig. 1. The detailed derivation of $I_{\text{corrected}}$ is described later. These values under ambient pressure and hydrostatic pressures of $P = 0.4$, 0.6, 0.7, 0.75, and 0.8 GPa were determined by a preliminary experiment (see Table I).

III. RESULTS

Figure 2 shows the corrected intensities obtained under ambient pressure. In the ground state ($T = 4$ K), reflections

TABLE I. Parameters A and B under different hydrostatic pressures.

Pressure (GPa)	A	B
Ambient pressure	5.0	0.7×10^{-4}
0.4	1.5	0.7×10^{-4}
0.6	1.5	1.5×10^{-4}
0.7	0.2	0.1×10^{-4}
0.75	0.2	0.1×10^{-4}
0.8	1.1	1.0×10^{-4}

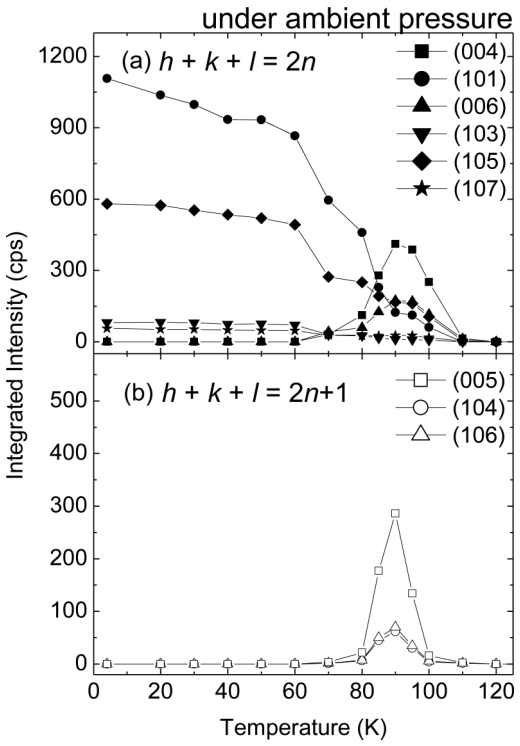

FIG. 2. Temperature dependence of the integrated intensities of typical peak positions under ambient pressure. (a) Peak positions at $h + k + l = 2n$ arise from both nuclear reflections and magnetic reflections from ferromagnetic structures: solid squares (004), solid circles (101), solid triangles (006), solid inverted triangles (103), solid diamonds (105), and solid stars (107). (b) Peak positions at $h + k + l = 2n + 1$ arise from magnetic reflections from antiferromagnetic structures: open squares (005), open circles (104), and open triangles (106).

exist from $h + k + l = 2n$, while those from $h + k + l = 2n + 1$ are missing. This means that the ground state is a ferromagnetic structure. As seen in the figure, however, $00l$ reflections from $h + k + l = 2n$ are missing, which is discussed in Sec. IV. At $T < 70$ K, the magnetic structure is ferromagnetic because the reflections from $h + k + l = 2n$ exist while those from $h + k + l = 2n + 1$ are missing. At $70\ \text{K} \leqslant T < 120$ K, the reflections from $h + k + l = 2n$ and $h + k + l = 2n + 1$ both exist. This means that the magnetic structure is complicated, exhibiting both ferromagnetic and antiferromagnetic characteristics, as described in Sec. IV. Figure 3 shows the corrected intensities obtained under a hydrostatic pressure of 0.6 GPa. The temperature dependence of intensities is the same as that under ambient pressure except that the $00l$ reflections from $h + k + l = 2n$ are missing at $70\ \text{K} \leqslant T < 90$ K. Thus, the magnetic structure is ferromagnetic at $T < 70$ K and becomes complicated and exhibits both ferromagnetic and antiferromagnetic characteristics at $70\ \text{K} \leqslant T < 120$ K.

Figure 4 shows the corrected intensities obtained under a hydrostatic pressure of 0.8 GPa. At $60\ \text{K} \leqslant T < 95$ K, the temperature dependence of intensities is the same as that under $P = 0.6$ GPa, while the temperature dependence of intensities is different from that under $P = 0.6$ GPa at $95\ \text{K} \leqslant T < 120$ K. At $95\ \text{K} \leqslant T < 120$ K, the magnetic

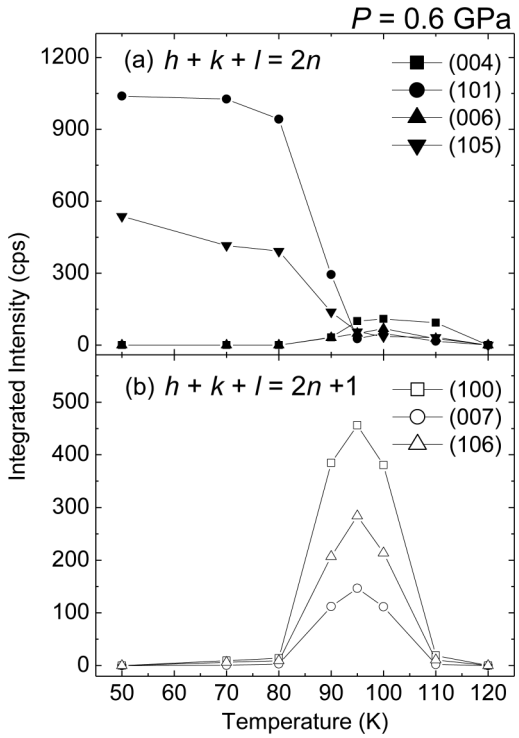

FIG. 3. Temperature dependence of the integrated intensities of typical peak positions under hydrostatic pressure of $P = 0.6$ GPa. (a) Peak positions at $h + k + l = 2n$: solid squares (004), solid circles (101), solid triangles (006), and solid inverted triangles (105). (b) Peak positions at $h + k + l = 2n + 1$: open squares (100), open circles (007), and open triangles (106).

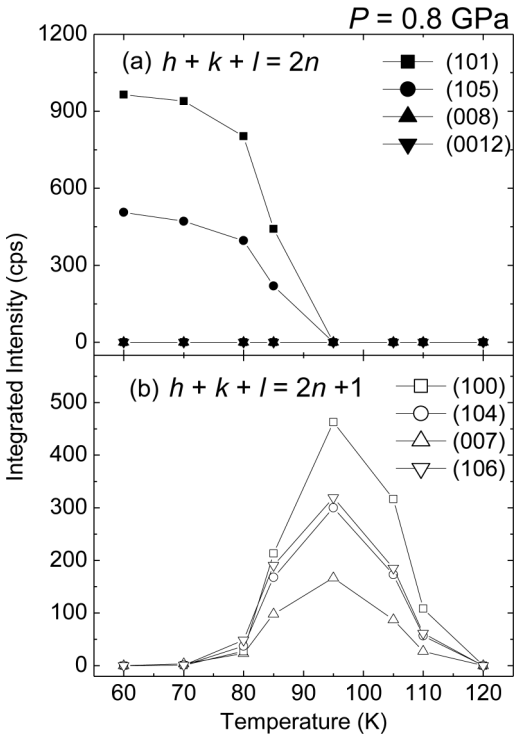

FIG. 4. Temperature dependence of the integrated intensities of typical peak positions under hydrostatic pressure of $P = 0.8$ GPa. (a) Peak positions at $h + k + l = 2n$: solid squares (101), solid circles (105), solid triangles (008), and solid inverted triangles (0012). (b) Peak positions of $h + k + l = 2n + 1$: open squares (100), open circles (104), open triangles (007), and open inverted triangles (106).

structure is antiferromagnetic because the reflections from $h + k + l = 2n$ are missing while those from $h + k + l = 2n + 1$ exist.

The hydrostatic pressure dependence of the magnetic structure in $La_{1.37}Sr_{1.63}Mn_2O_7$ obtained from the results under ambient pressure and under hydrostatic pressures of $P = 0.4$, 0.6, 0.7, 0.75, and 0.8 GPa are shown in Fig. 5 with the complicated magnetic structure described earlier referred to as a CAFM (canted-antiferromagnetic) structure as will be discussed in detail later.

IV. DISCUSSION

In this section, we analyze the magnetic structures under ambient pressure and hydrostatic pressures of $P = 0.4, 0.6, 0.7$, 0.75, and 0.8 GPa as follows. The total scattering cross-section $\frac{d\sigma}{d\Omega}$ is given by[21]

$$\frac{d\sigma}{d\Omega} = \frac{d\sigma_{\text{nuc.}}}{d\Omega} + \frac{d\sigma_{\text{mag.}}}{d\Omega}, \tag{2}$$

where $\frac{d\sigma_{\text{nuc.}}}{d\Omega}$ is the nuclear scattering cross section and $\frac{d\sigma_{\text{mag.}}}{d\Omega}$ is the magnetic scattering cross section. $\frac{d\sigma_{\text{nuc.}}}{d\Omega}$ is given by

$$\frac{d\sigma_{\text{nuc.}}}{d\Omega} = N\frac{(2\pi)^3}{v_0}\left[\sum_{j=1}^{n}\langle b\rangle_j \exp(i\,\boldsymbol{Q}\cdot\boldsymbol{R}_j)\right]^2 \sum_{\tau}\delta(\boldsymbol{Q}-\boldsymbol{\tau}), \tag{3}$$

where N is the number of unit cells in the crystal, v_0 is the volume of the unit cell, n is the number of atoms in the unit cell ($n = 24$), $\langle b\rangle_j$ is the average atomic scattering amplitude, $\boldsymbol{Q}$ is the scattering vector, $\boldsymbol{R}_j$ is the position vector from the origin to the jth atom in the unit cell, δ is the Dirac δ function, and $\boldsymbol{\tau}$ is the reciprocal lattice vector.

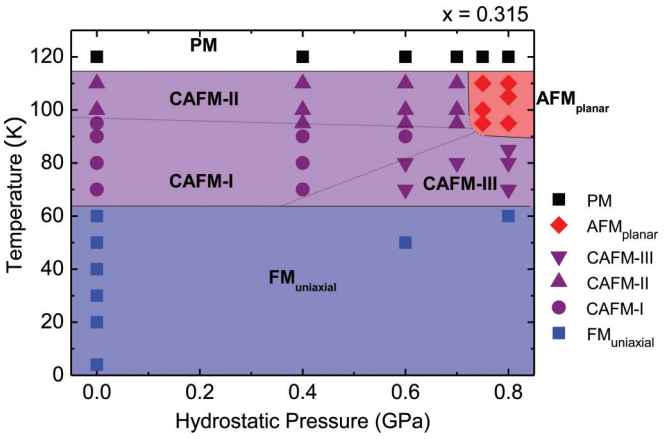

FIG. 5. (Color online) Magnetic phase diagram of $La_{1.37}Sr_{1.63}Mn_2O_7$ under hydrostatic pressures of up to 0.8 GPa: solid squares, $FM_{uniaxial}$ structure; solid circles, CAFM-I structure; solid triangles, CAFM-II structure; solid inverted triangles, CAFM-III structure; solid diamonds, AFM_{planar} structure; and open squares, paramagnetic (PM) structure. The phase boundary between AFM and CAFM structures is not yet clear. Further work is required.

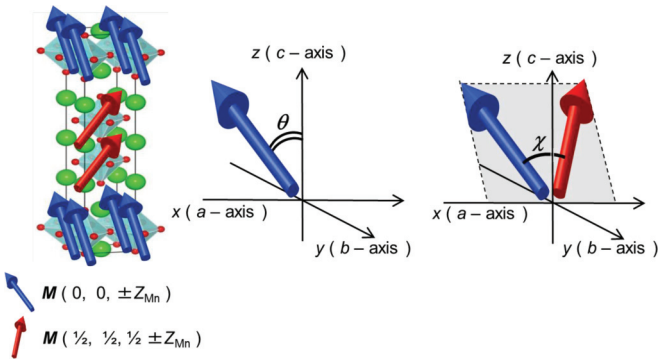

FIG. 6. (Color online) Schematic view of a magnetic structure model. Magnetic moment in the double layers is aligned in the same direction; θ represents the angle between the c axis and $\boldsymbol{M}_{0,0,\pm Z_{\mathrm{Mn}}}$ [Z_{Mn} is the z coordinate (c axis) for a Mn ion] and is assumed to be the same as the angle between the c axis and $\boldsymbol{M}_{1/2,1/2,1/2\pm Z_{\mathrm{Mn}}}$; χ represents the angle between $\boldsymbol{M}_{0,0,\pm Z_{\mathrm{Mn}}}$ and $\boldsymbol{M}_{1/2,1/2,1/2\pm Z_{\mathrm{Mn}}}$.

We assume that the unit cell of the magnetic structure is the same as that of the crystal structure, giving

$$\frac{d\sigma_{\mathrm{mag.}}}{d\Omega} = N\frac{(2\pi)^3}{v_0}\left[\sum_{j=1}^{n_m} p\boldsymbol{q}_j \exp(i\,\boldsymbol{Q}\cdot\boldsymbol{R}_j)\right]^2 \sum_{\tau}\delta(\boldsymbol{Q}-\boldsymbol{\tau}), \tag{4}$$

$$p = \left(\frac{\gamma e^2}{mc^2}\right)\cdot M\cdot f_{\mathrm{Mn}}(\boldsymbol{Q}), \tag{5}$$

and

$$\boldsymbol{q}_j = \hat{\boldsymbol{M}}_j - (\hat{\boldsymbol{M}}_j\cdot\hat{\boldsymbol{Q}})\hat{\boldsymbol{Q}}, \tag{6}$$

where n_m is the number of magnetic atoms in the unit cell ($n_m = 4$), p is the magnetic scattering amplitude, $\boldsymbol{q}_j$ is the $\boldsymbol{q}$ factor of the jth Mn ion, γ is the gyromagnetic ratio, e is the charge of an electron, m is the mass of an electron, c is the speed of light, M is the absolute value of the magnetic moment, $f_{\mathrm{Mn}}(\boldsymbol{Q})$ is the magnetic form factor, $\hat{\boldsymbol{M}}_j$ is the unit vector of $\boldsymbol{M}_j$, which is the magnetic moment of the jth Mn ion, and $\hat{\boldsymbol{Q}}$ is the unit vector of $\boldsymbol{Q}$. Substituting Eqs. (5) and

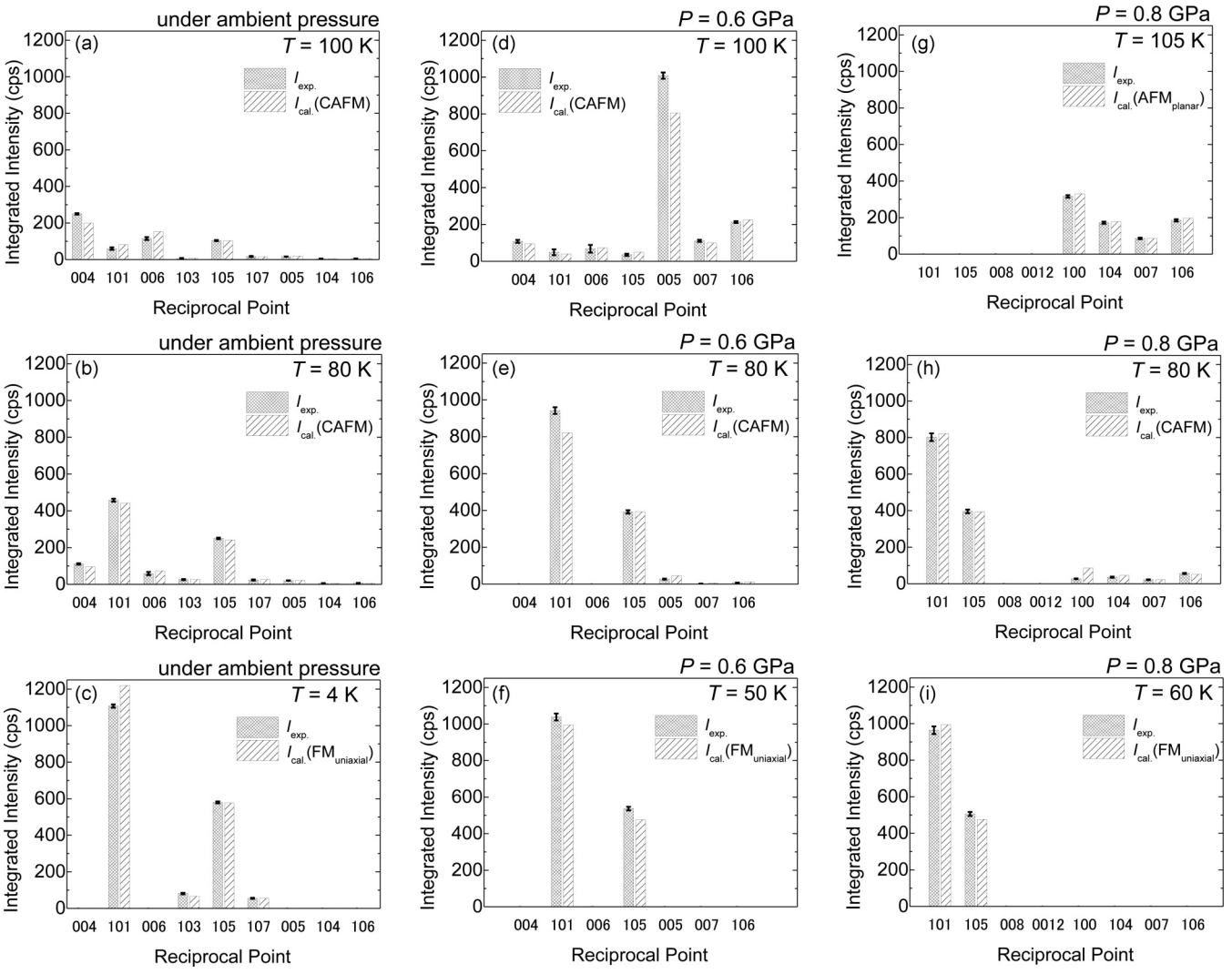

FIG. 7. Typical fitting results for (a)–(c) ambient pressure, (d)–(f) 0.6 GPa, and (g)–(i) 0.8 GPa for determining M, θ, and χ.

(6) into the magnetic structure factor in Eq. (4), we obtain

$$\sum_{j=1}^{n_m} p\boldsymbol{q}_j \exp(i\,\boldsymbol{Q}\cdot\boldsymbol{R}_j) = 0.269\times 10^{-12} f_{\mathrm{Mn}}(\boldsymbol{Q})\cdot M\cdot\sum_{j=1}^{n_m}\boldsymbol{q}_j\exp(i\,\boldsymbol{Q}\cdot\boldsymbol{R}_j), \quad (7)$$

where we assume the magnetic structure model shown in Fig. 6 in which the magnetic moments in the double layers are aligned in the same direction, θ represents the angle between the c axis and $\boldsymbol{M}_{0,0,\pm Z_{\mathrm{Mn}}}$ [Z_{Mn} is the z coordinate (c axis) for the Mn ions], which is assumed to be the same as the angle between the c axis and $\boldsymbol{M}_{1/2,1/2,1/2\pm Z_{\mathrm{Mn}}}$, and χ represents the angle between $\boldsymbol{M}_{0,0,\pm Z_{\mathrm{Mn}}}$ and $\boldsymbol{M}_{1/2,1/2,1/2\pm Z_{\mathrm{Mn}}}$ and is expressed by

$$\chi = \cos^{-1}\left(\frac{\boldsymbol{M}_{0,0,\pm Z_{\mathrm{Mn}}}\cdot\boldsymbol{M}_{1/2,1/2,1/2\pm Z_{\mathrm{Mn}}}}{M^2}\right). \quad (8)$$

In the above situation, Eq. (7) can be expressed by

$$\sum_{j=1}^{n_m} p\boldsymbol{q}_j \exp(i\,\boldsymbol{Q}\cdot\boldsymbol{R}_j) = 5.38\times 10^{-13} f_{\mathrm{Mn}}(\boldsymbol{Q})\cdot M\cdot(\boldsymbol{q}_{0,0,\pm Z_{\mathrm{Mn}}}+\boldsymbol{q}_{1/2,1/2,1/2\pm Z_{\mathrm{Mn}}})\cdot\cos(2\pi Z_{\mathrm{Mn}} l), \quad (9)$$

where $\boldsymbol{q}_{0,0,\pm Z_{\mathrm{Mn}}}$ and $\boldsymbol{q}_{1/2,1/2,1/2\pm Z_{\mathrm{Mn}}}$ are the $\boldsymbol{q}$ factors for $\boldsymbol{M}_{0,0,\pm Z_{\mathrm{Mn}}}$ and $\boldsymbol{M}_{1/2,1/2,1/2\pm Z_{\mathrm{Mn}}}$, respectively. Assuming the magnetic domains are equivalent, we have

$$\left[\sum_{j=1}^{n_m} p\boldsymbol{q}_j \exp(i\,\boldsymbol{Q}\cdot\boldsymbol{R}_j)\right]^2 = [5.38\times 10^{-13} f_{\mathrm{Mn}}(\boldsymbol{Q})\cdot M\cdot\cos(2\pi Z_{\mathrm{Mn}} l)]^2\cdot\left[1-\left(\frac{1}{2}\frac{h^2+k^2}{a^2}\sin^2\theta+\frac{l^2}{c^2}\cos^2\theta\right)d_{hkl}^2\right]. \quad (10)$$

Substituting Eq. (10) into Eq. (4), we obtain the magnetic scattering cross section,

$$\frac{d\sigma_{\mathrm{mag.}}}{d\Omega} = N\frac{(2\pi)^3}{v_0}[5.38\times 10^{-13} f_{\mathrm{Mn}}(\boldsymbol{Q})\cdot M\cdot\cos(2\pi Z_{\mathrm{Mn}} l)]^2\cdot\left[1-\left(\frac{1}{2}\frac{h^2+k^2}{a^2}\sin^2\theta+\frac{l^2}{c^2}\cos^2\theta\right)d_{hkl}^2\right]. \quad (11)$$

Considering the Lorentz factor gives the following calculated magnetic peak intensity $I_0(\boldsymbol{Q})$:

$$I_0(\boldsymbol{Q}) = \frac{d\sigma_{\mathrm{mag.}}}{d\Omega}\cdot\frac{1}{\sin 2\Theta} = N\frac{(2\pi)^3}{v_0}[5.38\times 10^{-13} f_{\mathrm{Mn}}(\boldsymbol{Q})\cdot M\cdot\cos(2\pi Z_{\mathrm{Mn}} l)]^2\cdot\left[1-\left(\frac{1}{2}\frac{h^2+k^2}{a^2}\sin^2\theta+\frac{l^2}{c^2}\cos^2\theta\right)d_{hkl}^2\right]\cdot\frac{1}{\sin 2\Theta}, \quad (12)$$

where $1/\sin 2\Theta$ is the Lorentz factor.

Under the above assumptions, the magnetic structure is governed by the parameters M, θ, and χ. The parameters M, θ, and χ are determined by fitting the calculated peak intensities to the experimental values $I_{\mathrm{corrected}}$. Typical fitting results are shown in Fig. 7 and the obtained parameters are summarized in Figs. 8(a)–8(c).

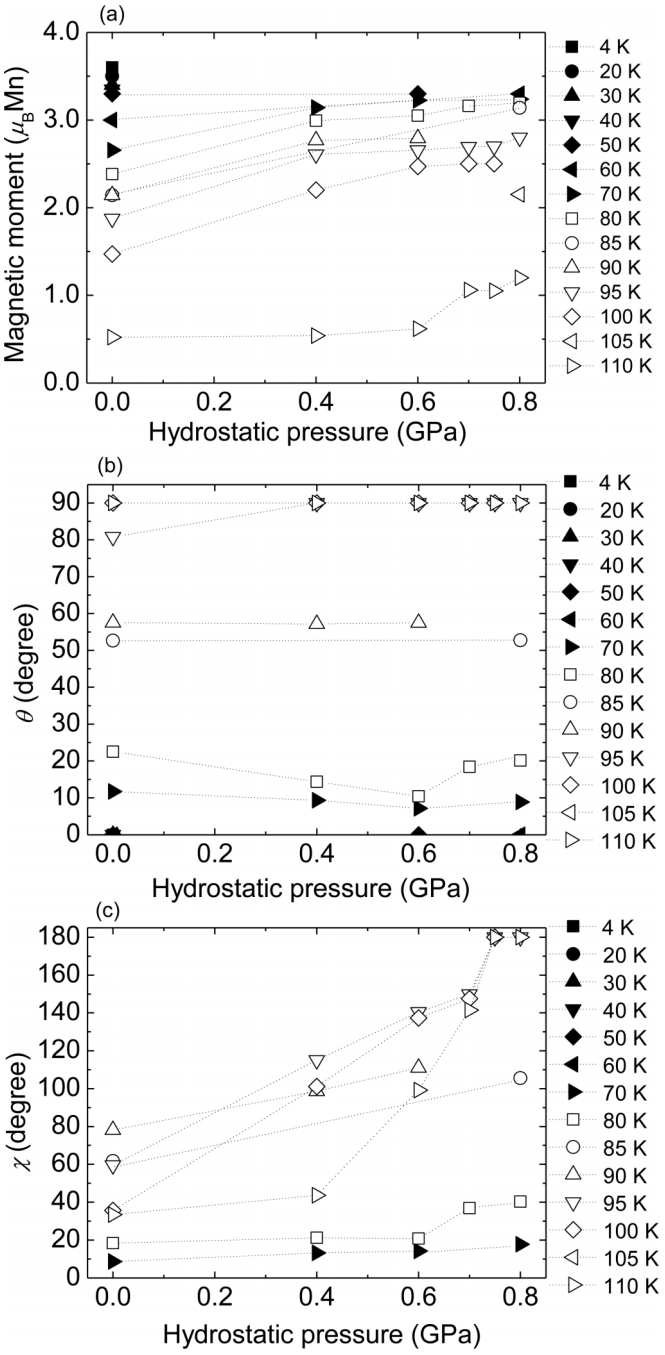

FIG. 8. Hydrostatic pressure dependence of (a) M, (b) θ, and (c) χ.

As Fig. 8 shows, with increasing hydrostatic pressure, M increases slightly at 4 K $\leqslant T <$ 120 K, θ is almost constant at 4 K $\leqslant T <$ 120 K, and χ is almost constant at $T <$ 85 K and drastically increases at 85 K $\leqslant T <$ 120 K. These results indicate that the hydrostatic pressure has a particularly strong effect on the value of χ in the exited states. Using the obtained values of M, θ, and χ, we can construct the magnetic phase diagram of $La_{1.37}Sr_{1.63}Mn_2O_7$ under hydrostatic pressure with the results as shown in Fig. 5. The ground state ($T = 4$ K) is the FM_{uniaxial} structure in the pressure

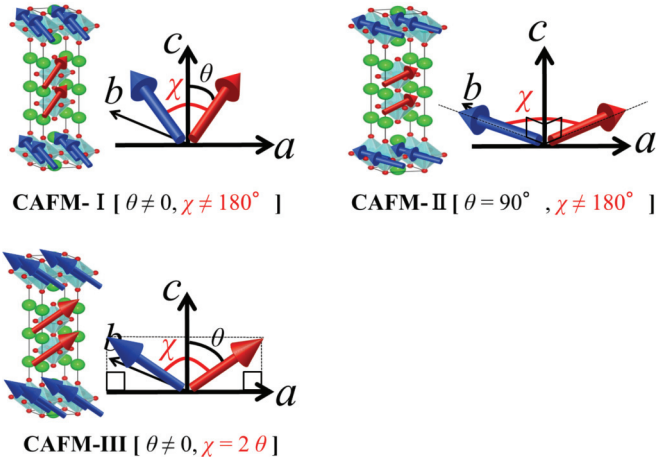

FIG. 9. (Color online) Schematic view of the canted magnetic structures. θ represents the angle between the c axis and $\boldsymbol{M}_{0,0,\pm Z_{\mathrm{Mn}}}$ and the angle between the c axis and $\boldsymbol{M}_{1/2,1/2,1/2\pm Z_{\mathrm{Mn}}}$ [Z_{Mn} is the z coordinate (c axis) for a Mn ion], and χ represents the angle between $\boldsymbol{M}_{0,0,\pm Z_{\mathrm{Mn}}}$ and $\boldsymbol{M}_{1/2,1/2,1/2\pm Z_{\mathrm{Mn}}}$.

range examined where the magnetic moment is parallel to the c axis. Under hydrostatic pressures of $P < 0.75$ GPa, the $\mathrm{FM_{uniaxial}}$ structure changes to a canted antiferromagnetic (CAFM) structure at approximately 70 K and the CAFM structure directly changes to a paramagnetic (PM) structure at approximately 120 K. Under hydrostatic pressures of $0.75\ \mathrm{GPa} \leqslant P \leqslant 0.8$ GPa, the $\mathrm{FM_{uniaxial}}$ structure changes to a CAFM structure at approximately 70 K, and the CAFM structure changes to a PM structure at approximately 120 K via an antiferromagnetic ($\mathrm{AFM_{planar}}$) structure at approximately 95 K, where the magnetic moment lies in the ab plane. The $\mathrm{AFM_{planar}}$ structure in the present study is different from the AFM structure (in the ground state of $x = 0.48$) reported by Kubota *et al.*, in which the magnetic moments were antiparallel to each other in the double layers.

Incidentally, the CAFM structure can be classified into three groups by the values of θ and χ, as shown in Fig. 9. The CAFM-I structure has magnetic moments with $\theta \neq 0°$ and $\chi \neq 180°$, the CAFM-II structure has magnetic moments in the ab plane with $\chi \neq 180°$, and the CAFM-III structure has magnetic moments in a plane perpendicular to the ab plane with $\chi = 2\theta$. In the excited states above 60 K, as the hydrostatic pressure increases, the CAFM-I and CAFM-II structures with $\chi \neq 180°$ change to the CAFM-III and $\mathrm{AFM_{planar}}$ structures with $\chi = 180°$, respectively.

The CAFM structure obtained in the present study does not arise because of magnetic phase separation or a helical magnetic structure (core skyrmion). The reason is that if we assume magnetic phase separation, the magnetic moment of the Mn ion [typical value of 4.10 (μ_{B}/Mn ion) at 80 K, 0.8 GPa] becomes much larger than the spontaneous magnetization obtained from the M-H curve [typical value of 3.23 (μ_{B}/Mn ion) at 80 K, 0.8 GPa], which is shown in Fig. 10. Furthermore, there are no peaks found by scanning the hkl from 001 to 002. This suggests that there is no helical magnetic structure along the c axis. Therefore, the CAFM structure in the present study is an appropriate structure for explaining the experimental peak intensities of the magnetic reflections.

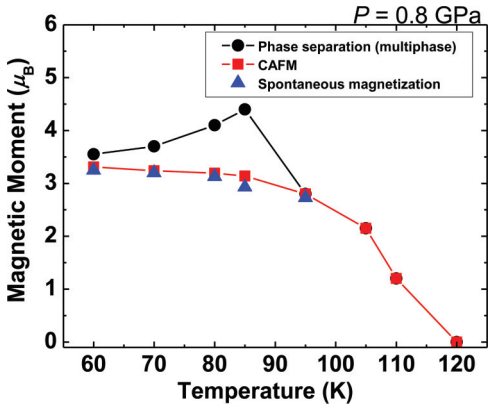

FIG. 10. (Color online) Temperature dependence of M under $P = 0.8$ GPa. Black circles, red squares, and blue triangles represent the magnetic moments of phase separation, a CAFM structure, and spontaneous magnetization, respectively.

The present result indicates that hydrostatic pressure enhances the antiferromagnetic interaction between neighboring double layers. This change seems to be closely related to the distortion of the MnO_6 octahedra. Argyriou *et al.* reported that the MnO_6 octahedra in $La_{1.2}Sr_{1.8}Mn_2O_7$ ($x = 0.4$) shrink slightly along the c axis at 100 K due to the increase in hydrostatic pressure.[18] This causes an increase in the occupancy of the x^2-y^2 orbital relative to the $3z^2$-r^2 orbital, which influences on the competition between the ferromagnetic interaction and the antiferromagnetic interaction via the variation in transfer integral along the c axis. On the other hand, it seems that the ground state does not change under the application of hydrostatic pressures of up to 0.8 GPa. The reason is not clear, but this suggests the magnetic structure depends not only on the stability of the crystal field energy but also on other interactions, such as a magnetic dipole-dipole interactions.

V. SUMMARY

We have studied magnetic structures in $La_{1.37}Sr_{1.63}Mn_2O_7$ under hydrostatic pressures of up to 0.8 GPa by neutron diffraction measurement and have determined the magnetic phase diagram. As shown in the phase diagram, we have concluded that the ground state remains the $\mathrm{FM_{uniaxial}}$ structure at up to 0.8 GPa, whereas the CAFM-I and CAFM-II structures with $\chi \neq 180°$ in the excited states change to the CAFM-III and $\mathrm{AFM_{planar}}$ structures with $\chi = 180°$, respectively, with increasing hydrostatic pressure. This means that hydrostatic pressure enhances the antiferromagnetic interaction between neighboring double layers.

ACKNOWLEDGMENTS

This study was performed under the Common-Use Facility Program of JAEA, Priority Assistance for the Formation of Worldwide Renowned Centers of Research - The Global COE Program (Project: Center of Excellence for Advanced Structural and Functional Materials Design) and supported by the Ministry of Education, Culture, Sports, Science and Technology (MEXT), Japan.

*hirosuke.sonomura@mat.eng.osaka-u.ac.jp
†terai@mat.eng.osaka-u.ac.jp
‡kakesita@mat.eng.osaka-u.ac.jp
§osakabe.toyotaka@jaea.go.jp
‖kazuhisa.kakurai@jaea.go.jp

[1] S. N. Ruddlesden and P. Popper, Acta Crystallogr. **11**, 54 (1958).
[2] T. G. Perring, G. Aeppli, Y. Moritomo, and Y. Tokura, Phys. Rev. Lett. **78**, 3197 (1997).
[3] T. Kimura, Y. Tomioka, A. Asamitsu, and Y. Tokura, Phys. Rev. Lett. **81**, 5920 (1998).
[4] T. Fukumura, H. Sugawara, T. Hasegawa, K. Tanaka, H. Sakaki, T. Kimura, and Y. Tokura, Science **284**, 1969 (1999).
[5] T. Akimoto, Y. Moritomo, K. Ohoyama, S. Okamoto, S. Ishihara, S. Maekawa, and A. Nakamura, Phys. Rev. B **59**, R14153 (1999).
[6] D. N. Argyriou, J. F. Mitchell, P. G. Radaelli, H. N. Bordallo, D. E. Cox, M. Medarde, and J. D. Jorgensen, Phys. Rev. B **59**, 8695 (1999).
[7] Eun-Ok Chi, Kun-Pyo Hong, Young-Uk Kwon, N. P. Raju, J. E. Greedan, Jeong-Soo Lee, and Nam Hwi Hur, Phys. Rev. B **60**, 12867 (1999).
[8] Fan Zhong and Z. D. Wang, Phys. Rev. B **62**, 5297 (2000).
[9] J. F. Mitchell, C. D. Ling, J. E. Millburn, D. N. Argyriou, A. Berger, and M. Medarde, J. Appl. Phys. **89**, 6618 (2001).
[10] S. Okamoto, S. Ishihara and S. Maekawa, Phys. Rev. B **63**, 104401 (2001).
[11] K. Hirota, S. Ishihara, H. Fujioka, M. Kubota, H. Yoshizawa, Y. Moritomo, Y. Endoh, and S. Maekawa, Phys. Rev. B **65**, 064414 (2002).
[12] Y. Tokunaga, M. Tokunaga, and T. Tamegai, Physica B **329-333**, 908 (2003).
[13] M. Konoto, T. Kohashi, K. Koike, T. Arima, Y. Kaneko, T. Kimura, and Y. Tokura, Phys. Rev. Lett. **93**, 107201 (2004).
[14] Y. Tokunaga, T. Lottermoser, Y. Lee, R. Kumai, M. Uchida, T. Arima, and Y. Tokura, Nat. Mater. **5**, 937 (2006).
[15] T. Murata, T. Terai, T. Fukuda, and T. Kakeshita, J. Magn. Magn. Mater. **303**, 138 (2006).
[16] T. Murata, T. Terai, T. Fukuda, and T. Kakeshita, Mater. Sci. Forum **512**, 183 (2006).
[17] M. Kubota, H. Fujioka, K. Hirota, K. Ohoyama, Y. Moritomo, H. Yoshizawa, and Y. Endo, J. Phys. Soc. Jpn. **69**, 1606 (2000).
[18] D. N. Argyriou, J. F. Mitchell, J. B. Goodenough, O. Chmaissem, S. Short, and J. D. Jorgensen, Phys. Rev. Lett. **78**, 1568 (1997).
[19] T. Murata, T. Terai, T. Fukuda, and T. Kakeshita, in *Proceedings of the International Conference on Solid-Solid Phase Transformations in Inorganic Materials*, *2005*, edited by J. M. Howe, D. E. Laughlin, J. K. Lee, U. Dahmen, W. A. Soffa (TMS, Warrendale, 2005), Vol. 2, pp. 1007–1010.
[20] R.W. James, *The Optical Principles of the Diffraction of X-Rays* (Bell, London, 1954).
[21] G. L. Squires, *Introduction to the Theory of Thermal Neutron Scattering* (Dover, New York, 1978).